Supporting Information

PET-upcycled and Biobased Hyperbranched Polyesters for Self-healable and Flame-retardant Powder Coatings

Song Gu, Jingjing Du, Yaqiong Zhang, Wangcheng Liu, Gustavo de Figueiredo Brito, Yiding Cao, Baoming Zhao, Jinwen Zhang**

School of Mechanical and Materials Engineering, Composite Materials and Engineering Center,

Washington State University, Pullman, WA, 99164, USA

Table of contents

1. Aminolysis of PET

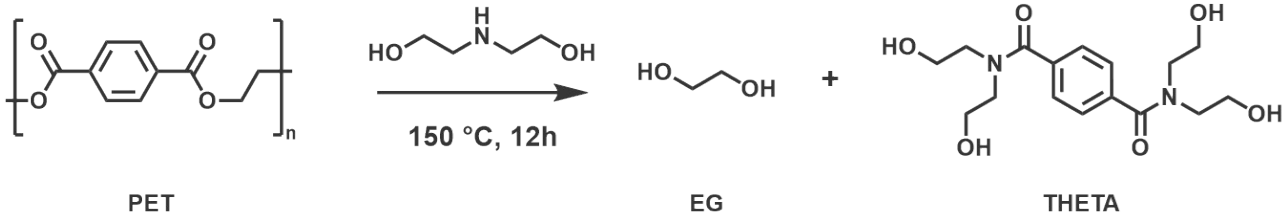

Scheme S1. Upcycling PET to N^1,N^1,N^4,N^4-tetrakis(2-hydroxyethyl) terephthalamide (THETA) by aminolysis in diethanolamine.

2. NMR spectra of THETA

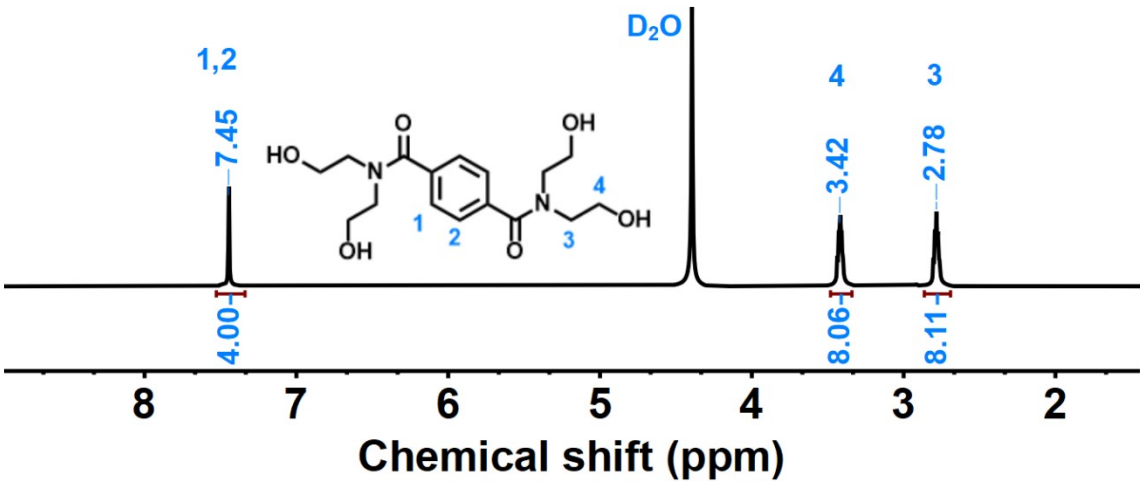

Figure S1. ^{1}H NMR (D_2O, 500 MHz) spectrum of THETA.

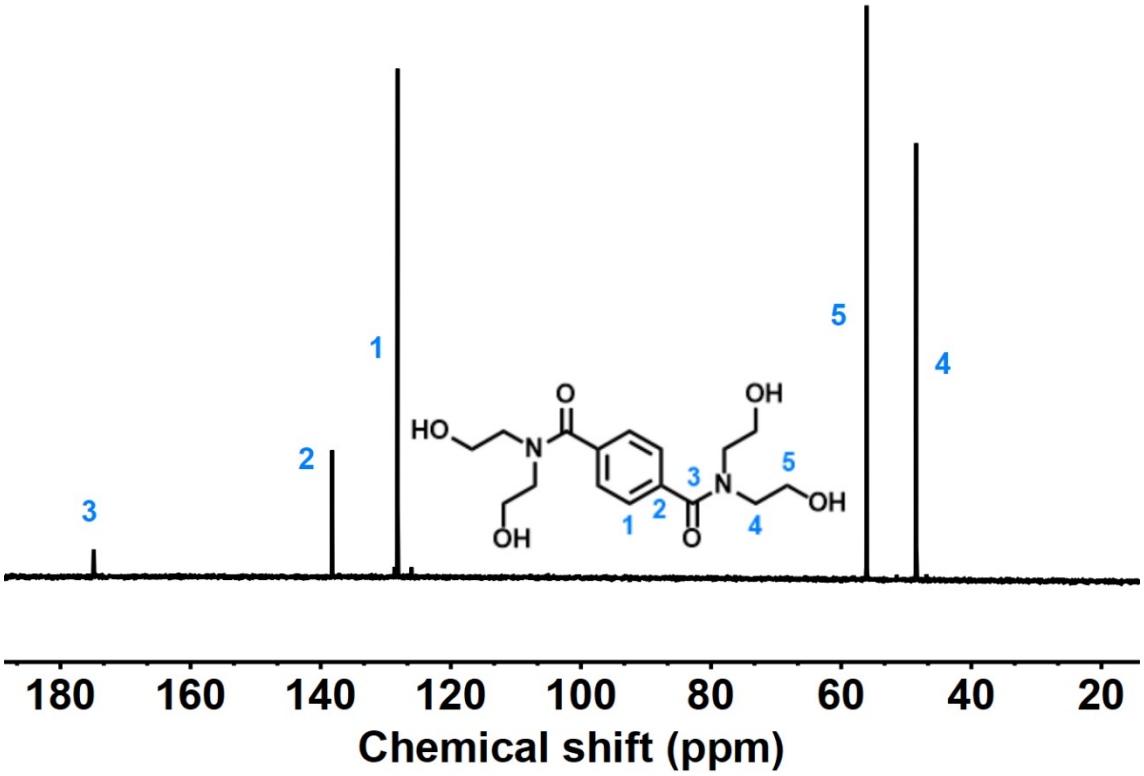

Figure S2. ^{13}C NMR (D_2O, 500 MHz) spectrum of THETA.

3. Melting point of THETA and REP

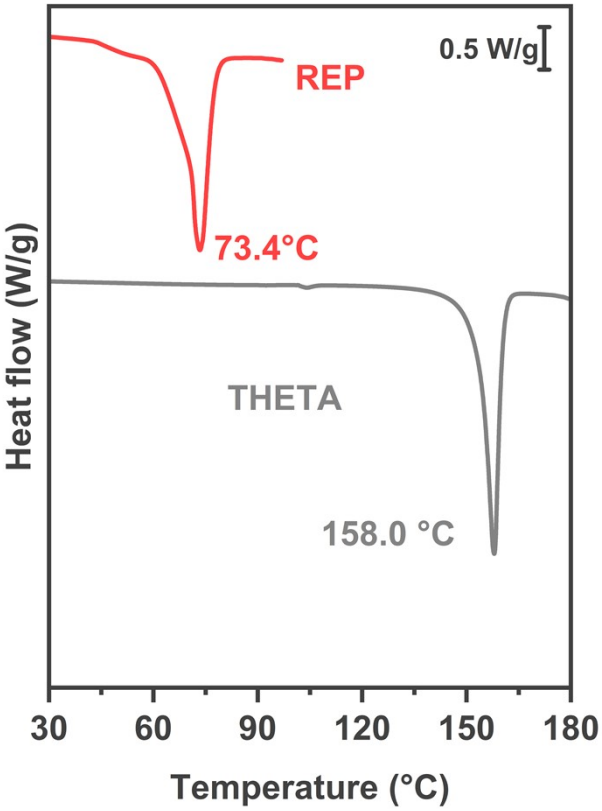

Figure S3. Melting point of THETA and REP measured using DSC at 10 °C/min.

4. Composition of HBPEs

Table S1. Composition of HBPEs, acid value, and the content of bio-based carbon and carbon from PET.

Sample	THETA (g)	DOPO-Itaconic acid (g)	SA (g)	BTCD (g)	Theor. AV[a] (mg KOH/g)	Actual AV (mg KOH/g)	Theor. HV[b] (mg KOH/g)	Actual HV (mg KOH/g)	Carbon from PET (%)	Bio-based carbon (%)
P-HBPE$_{0.25}$	25.00	20.35	5.20	0.51	51.93	34.56	155.78	143.86	25.00	20.00
P-HBPE$_{0.50}$	25.00	20.35	10.41	0.56	95.06	86.11	95.06	83.72	23.26	25.58
P-HBPE$_{0.75}$	25.00	20.35	15.61	0.61	131.45	119.38	43.82	39.58	21.74	30.43
P-HBPE$_{1.0}$	25.00	20.35	20.82	0.66	162.56	154.22	0	0.97	20.41	34.70
HBPE$_{0.50}$	25.00	0	17.35	0.42	128.04	100.31	128.04	119.13	33.33	33.33

[a]AV: acid value; [b]HV: hydroxyl value

5. Synthesis of P-HBPEs with different acid values

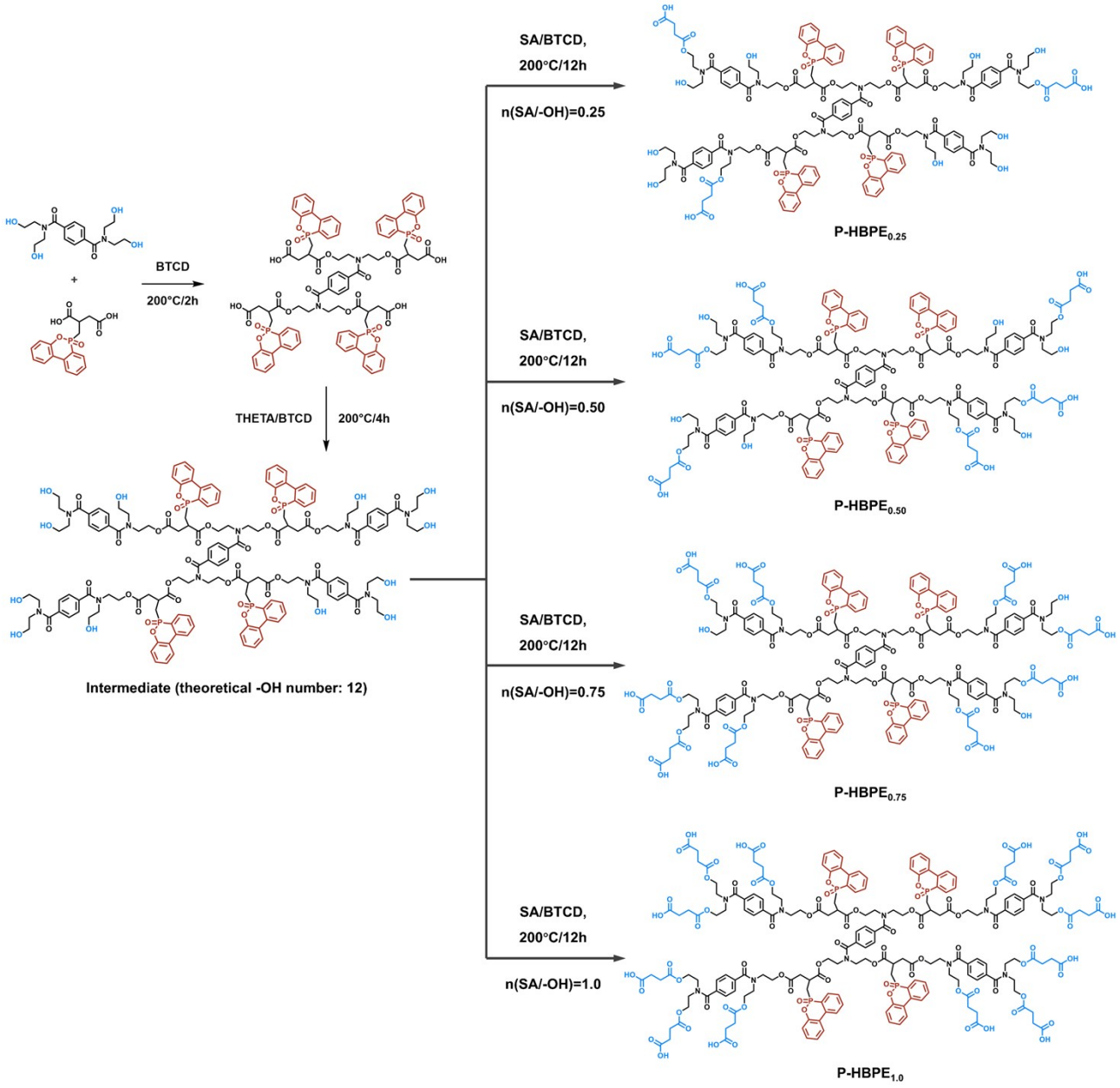

Figure S4. Preparation of P-HBPEs with variable acid values by adjusting the feed ratio of succinic acid.

6. NMR spectra of HBPEs

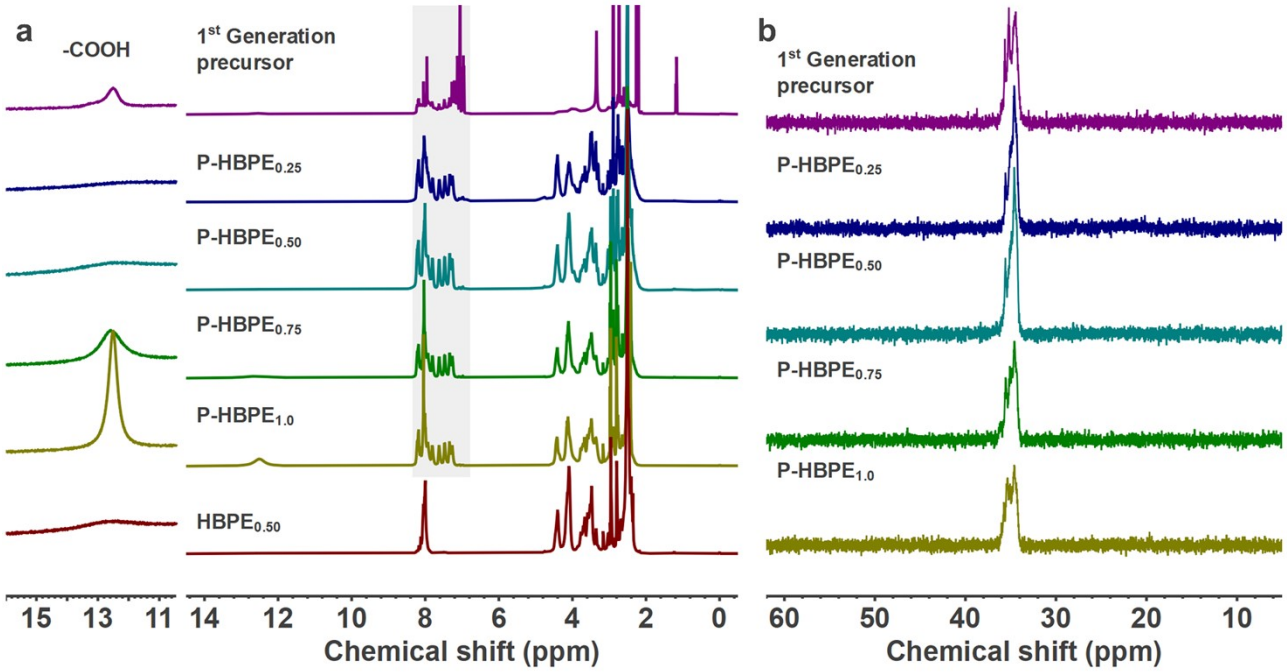

Figure S5. (a) ^{1}H NMR (DMSO-d6, 500 MHz) and (b) ^{31}P NMR (DMSO-d6, 500 MHz) spectra of HBPEs.

7. Molecular weight of HBPEs

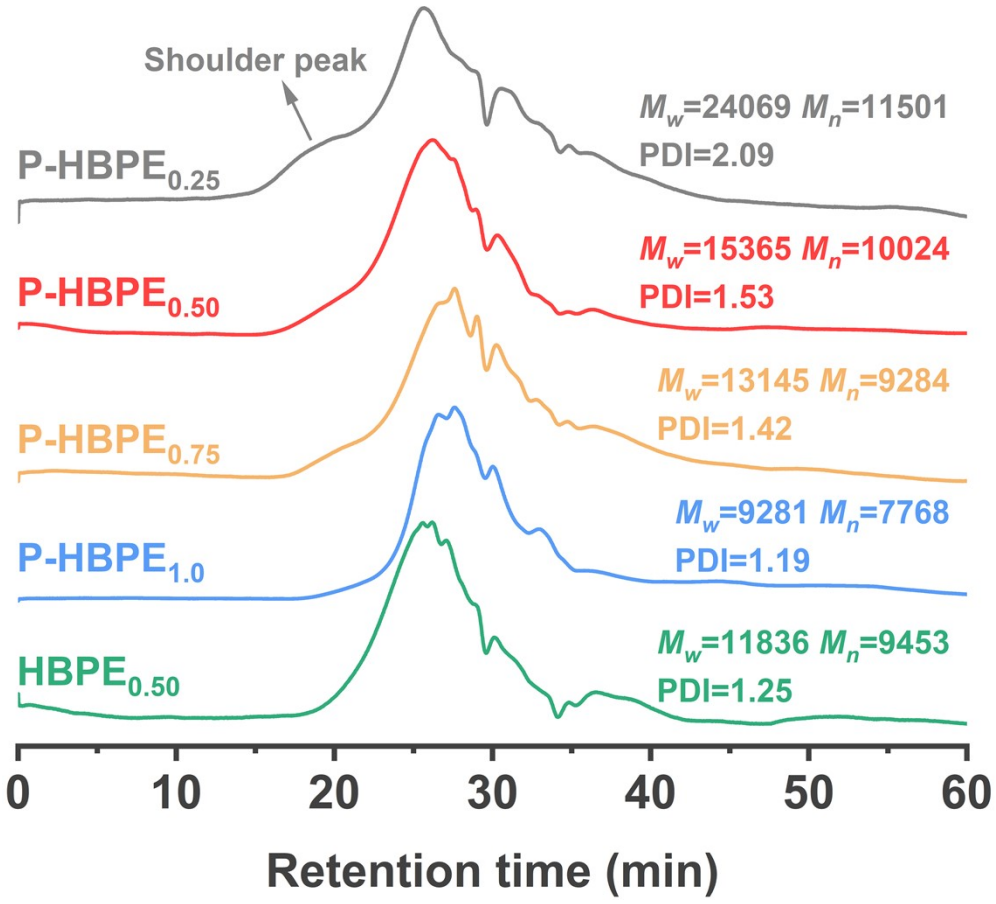

Figure S6. SEC traces of HBPEs.

Figure S6 shows the SEC traces of the HBPEs. As the acid value of the P-HBPEs increases, both the weight-average molecular weight (Mw) and number-average molecular weight (Mn) decrease gradually. In principle, a higher acid value corresponds to a higher SA feed, and the molecular weight would be expected to increase accordingly. The opposite trend observed here may arise from deviations between the designed and the effective stoichiometry during high-temperature polycondensation: it is difficult to maintain the intended equivalence of hydroxyl and carboxyl functionalities at each feeding step and to confine the reaction strictly to the targeted conversion. This effect is expected to be more significant for hydroxyl-rich formulations (P-HBPE$_{0.25}$, P-HBPE$_{0.50}$, and P-HBPE$_{0.75}$). During the final reaction with SA, the carboxyl groups intended to remain as terminal functionalities may still undergo further esterification with residual hydroxyl groups, thereby increasing the actual extent of polycondensation beyond the theoretical design. Consequently, samples with lower acid values can exhibit higher molecular weights. In addition, the SEC trace of

P-HBPE$_{0.25}$ displays a distinct shoulder at shorter retention times; similar shoulders are observed for P-HBPE$_{0.50}$ and P-HBPE$_{0.75}$, with progressively reduced intensity. Collectively, these results indicate that the experimentally measured molecular-weight trend across this series is opposite to that predicted from the nominal formulation.

8. Glass transition temperatures and temperature-dependent viscosity of HBPEs

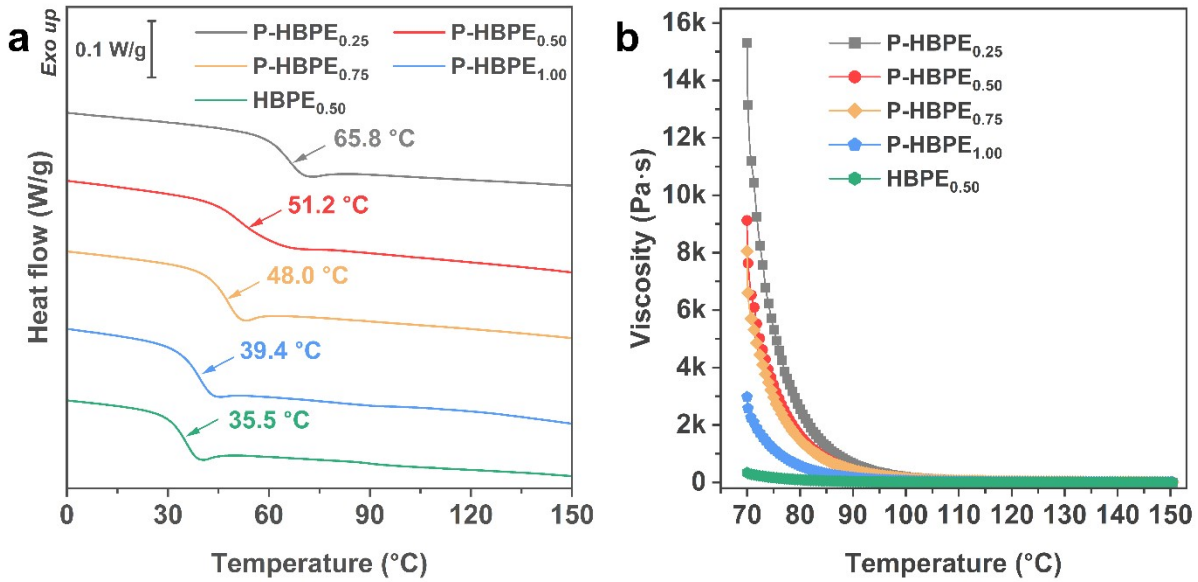

Figure S7. (a) Glass transition temperatures of HBPEs, (b) temperature-dependent viscosity curves of the corresponding HBPEs.

Table S2. Melt-viscosity comparison between the hyperbranched polyesters in this work and representative commercial powder-coating polyesters.

Polyester resin	Supplier	Intended use	Melt viscosity	Test condition
CRYLCOAT 1622-0	allnex	Hybrid powder coating	2.5 Pa·s	200 °C
CRYLCOAT 1627-0	allnex	Hybrid powder coating	4.0 Pa·s	200 °C
CRYLCOAT 1650-2	allnex	Hybrid powder coating	4.25 Pa·s	200 °C
CRYLCOAT 1702-0	allnex	Hybrid powder coating	5.3 Pa·s	200 °C
CRYLCOAT 1713-1	allnex	Hybrid powder coating	4.5 Pa·s	200 °C
REAFREE® 6402-T	Arkema	Polyester/epoxy hybrid powder coating	20-38 Pa·s	165 °C
REAFREE® 6460-T	Arkema	Polyester/epoxy hybrid powder coating	10-20 Pa·s	165 °C
REAFREE® 6480-T	Arkema	Polyester/epoxy hybrid powder coating	9-14 Pa·s	165 °C
P-HBPE	This work	Polyester/epoxy hybrid powder coating	0.7-3.0 Pa·s	150 °C

As shown in **Figure S7b**, the melt viscosities of the P-HBPE series decreased markedly with increasing temperature, indicating favorable thermal flowability over the temperature range relevant to powder-coating processing. Considered together with the viscosity–temperature profile of the HBPE resin itself, these results suggest that the hyperbranched polyester architecture is associated with relatively low melt viscosity, which is beneficial for melt flow and leveling. **Table S2** further compiles published melt-viscosity data for representative commercial polyester resins used in powder coatings. Because these commercial data were obtained under testing conditions different from those employed in this work, the comparison is intended for qualitative reference only. Even so, this comparison provides additional context supporting the low-viscosity nature of the hyperbranched polyester system developed here and its favorable implications for melt flow and leveling in powder-coating applications.

9. Synthesis of REP

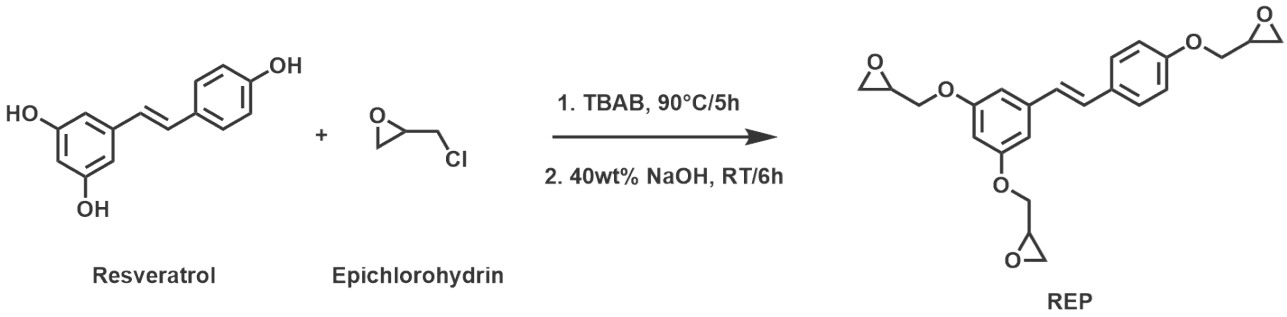

Scheme S2. Synthesis of REP.

10. NMR spectra of REP

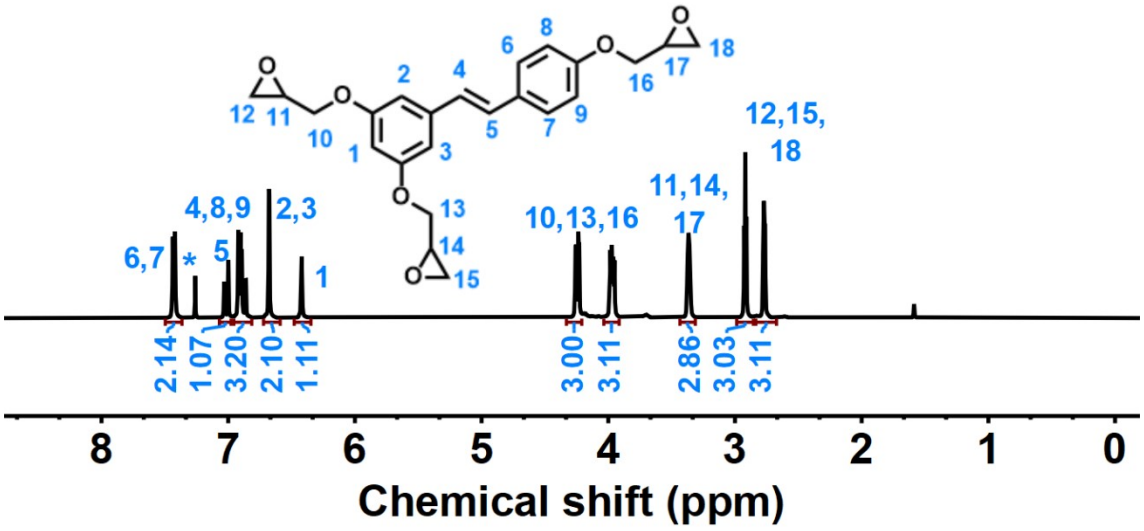

Figure S8. ^{1}H NMR ($CDCl_3$, 500 MHz) spectrum of REP.

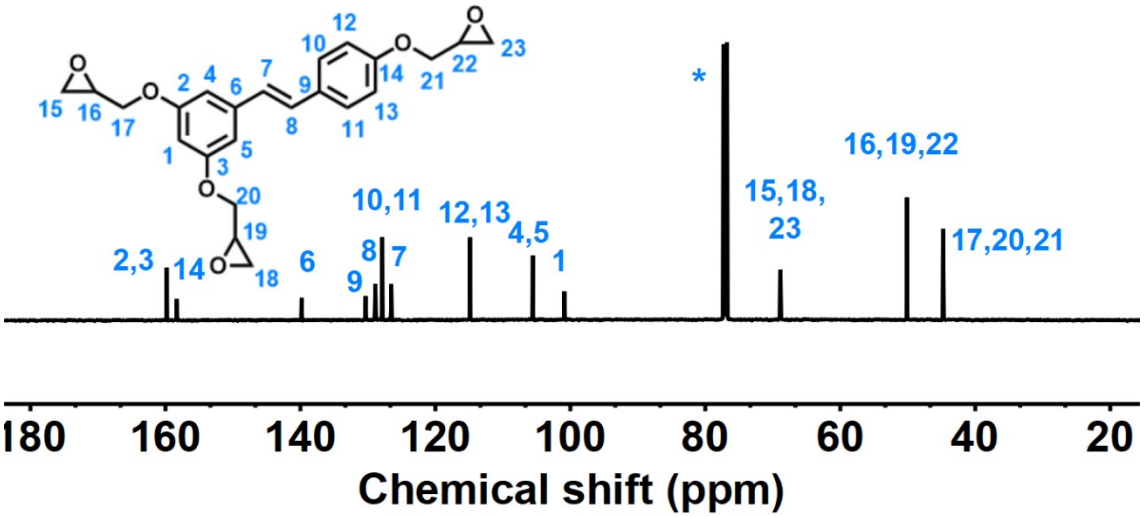

Figure S9. ^{13}C NMR ($CDCl_3$, 500 MHz) spectrum of REP.

11. Composition of HBPE-REP coating

Table S3. Composition of HBPE-REP, and the content of bio-based carbon and carbon from PET.

Sample	HBPE (g)	REP (g)	Leveling agent (g)	TiO_2 (20wt%, g)	Carbon from PET (%)	Bio-based carbon (%)
P-$HBPE_{0.25}$-REP	45.00	4.21	0.98	0	22.40	23.03
P-$HBPE_{0.50}$-REP	45.00	10.50	1.11	0	18.49	31.60
P-$HBPE_{0.75}$-REP	45.00	14.55	1.19	0	16.11	37.16
P-$HBPE_{1.0}$-REP	45.00	18.80	1.28	0	14.10	41.57
$HBPE_{0.50}$-REP	45.00	12.23	1.14	0	25.70	38.48
P-$HBPE_{0.50}$-REP/TiO_2	38.16	8.90	0.94	12	21.20	25.28

12. Curing behavior and thermal properties of HBPE-REP bulk resins

Table S4. Curing peak temperature, glass transition temperature, and TGA data of HBPE-REP.

Sample	T_p of curing (°C)	T_g (°C)	Gel content (%)	Swelling ratio	$T_{5\%}$ (°C)	$T_{d\ max}$ (°C)	Char yield (wt%)
P-HBPE$_{0.25}$-REP	154.2	67.7	70.3±2.1	2.73±0.16	275.9	381.2	22.6
P-HBPE$_{0.50}$-REP	143.3	68.8	97.9±1.6	1.55±0.08	277.4	372.7	27.4
P-HBPE$_{0.75}$-REP	133.9	68.2	98.3±1.2	1.51±0.07	279.7	368.0	30.3
P-HBPE$_{1.0}$-REP	130.5	67.8	98.2±1.5	1.56±0.05	278.3	369.0	31.2
HBPE$_{0.50}$-REP	130.9	45.3	98.5±0.8	1.53±0.03	272.6	328.5	23.1

13. Digital photographs of HBPEs, HBPE/REP, and HBPE/REP/TiO_2 blends

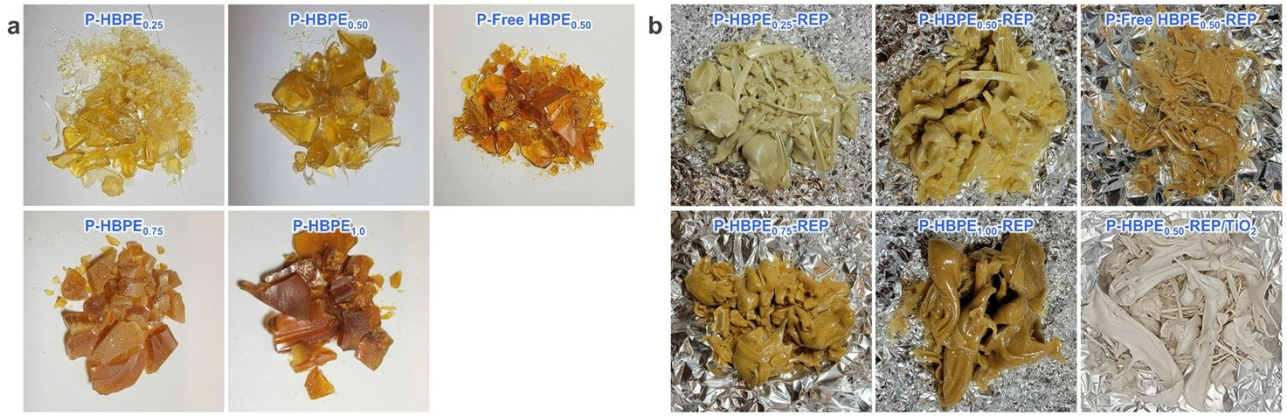

Figure S10. Digital photographs of (a) HBPEs, and (b) HBPE/REP, HBPE/REP/TiO_2 blends.

14. FTIR spectra of REP, HBPEs, and the HBPE-REP bulk resins

The FTIR spectra of $HBPE_{0.5}$, P-$HBPE_{0.50}$, and their bulk resins cured with REP are presented in **Figure S11**. Characteristic absorption bands observed at approximately 3400, 2855-2962, 1722, 1638-1671, and 1593 cm^{-1} correspond to hydroxyl groups, C-H stretching of methylene groups, ester carbonyls, amide groups, and C=C double bonds in the resveratrol moiety, respectively. This indicates that the bulk resins consist of hyperbranched polyesters and REP. Notably, the characteristic epoxy absorption band of REP around 906 cm^{-1} disappeared in the cured the $HBPE_{0.5}$-REP, demonstrating the participation of epoxy groups in the curing reaction. In contrast, the spectrum of P-$HBPE_{0.50}$ reveals an absorption band near 906 cm^{-1}, which is absent in $HBPE_{0.5}$. This band originates from the P-C bending vibration in the P-HBPE0.50 structure, and its absorption overlaps with the typical epoxy band in this region. Therefore, in the spectrum of the cured P-$HBPE_{0.50}$-REP sample, the residual absorption near 906 cm^{-1} is primarily attributed to the P-C vibration rather than unreacted epoxy groups, providing supporting evidence for the presence of phosphorus-containing structures in the resulting network structure.

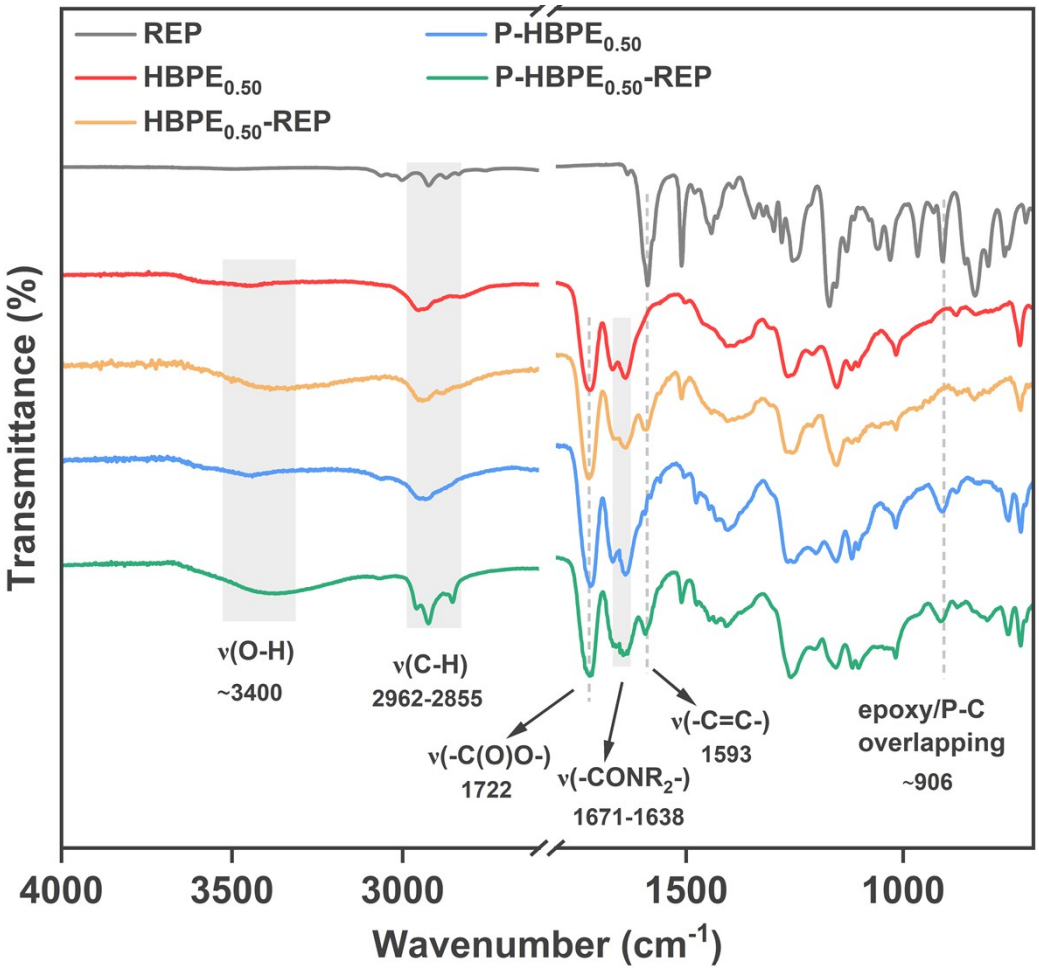

Figure S11. FTIR spectra of REP, HBPEs, and the HBPE-REP bulk resins.

15. Glass transition temperatures of cured resins from the steel plates

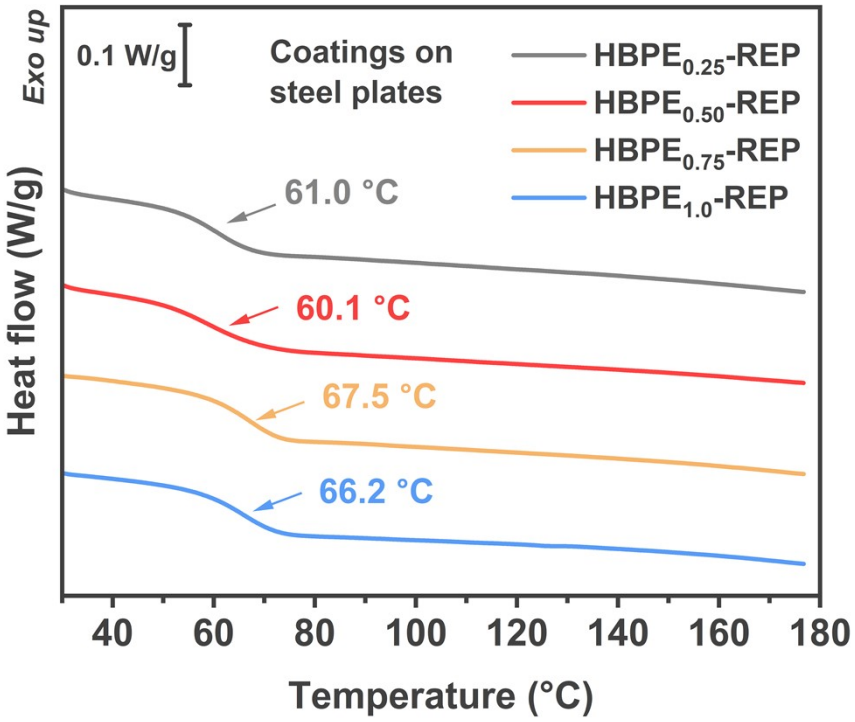

Figure S12. Glass transition temperatures of cured coating resins from the steel plates.

16. Self-healing and shape memory behavior

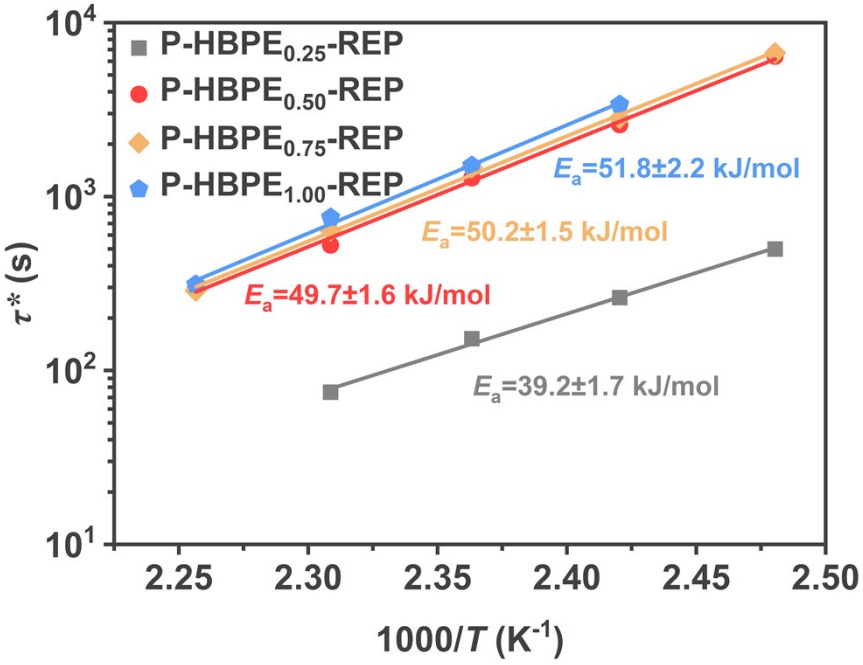

Figure S13. Arrhenius plot of the measured relaxation times.

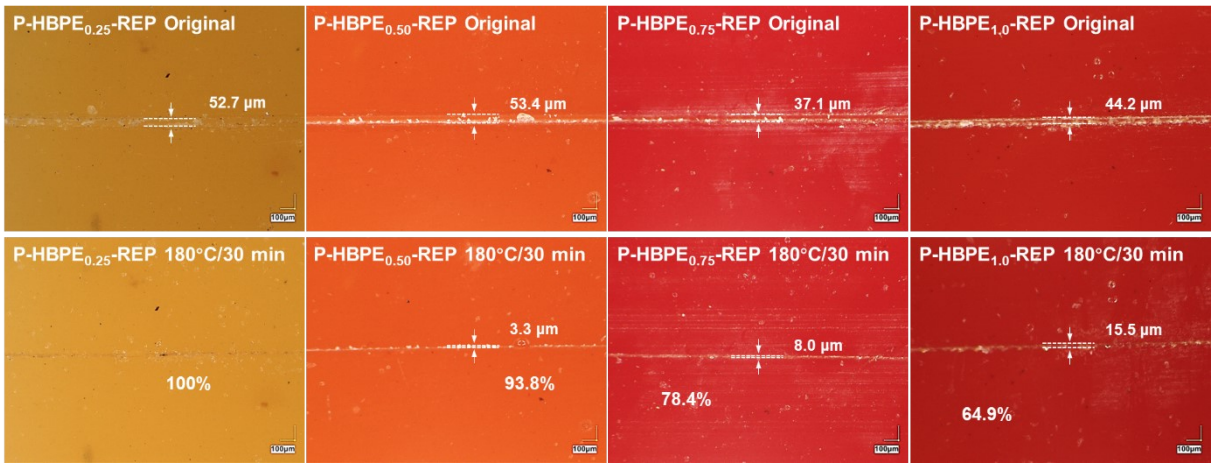

Figure S14. Optical microscopy images of P-HBPE-REPs self-healing at 180 °C for 30 min.

Figure S15. Shape memory behavior of P-HBPE$_{0.50}$-REP.

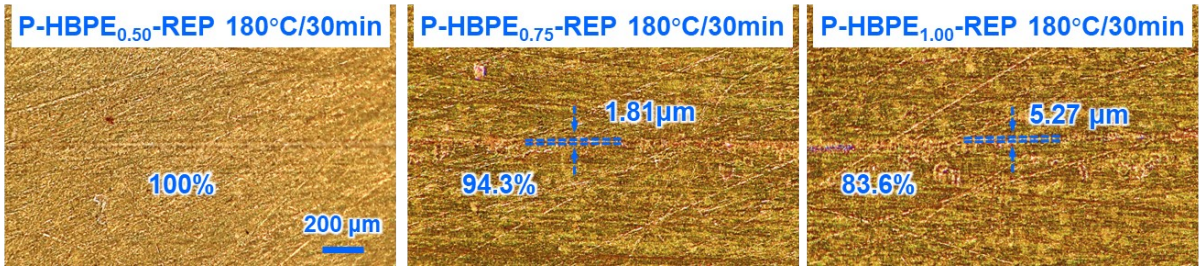

Figure S16. Optical microscopy images of P-HBPE$_{0.50}$-REP/steel, P-HBPE$_{0.75}$-REP/steel, and P-HBPE$_{1.0}$-REP/steel coating self-healing at 180°C for 30 min.

17. Photographs of aluminum panels, MDF, and basswood sheets spray-coated with P-HBPE$_{0.50}$-REP and P-HBPE$_{0.50}$-REP/TiO$_2$

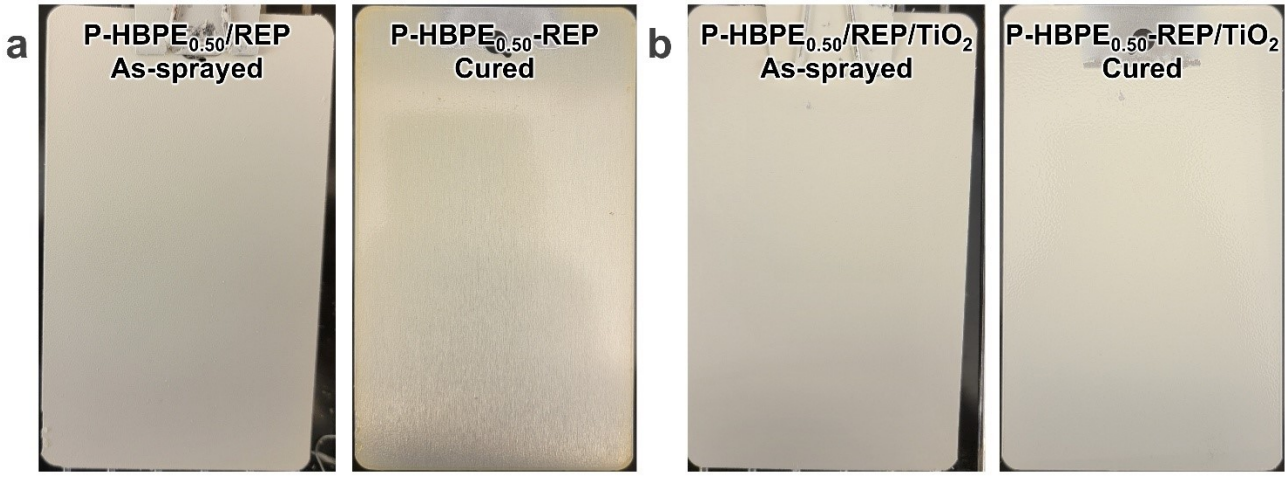

Figure S17. Photographs of aluminum panels spray-coated with P-HBPE$_{0.50}$-REP and P-HBPE$_{0.50}$-REP/TiO$_2$ before and after curing.

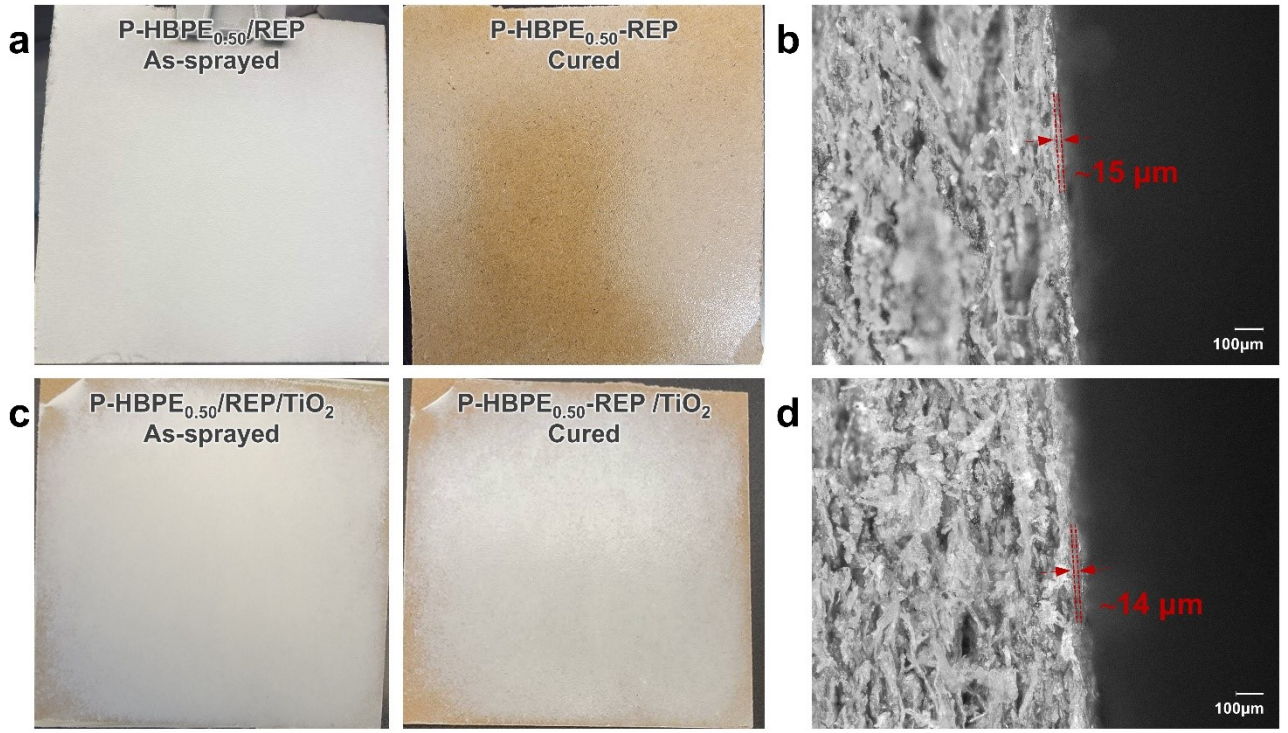

Figure S18. (a, c) Photographs of MDF coated with P-HBPE$_{0.50}$-REP and P-HBPE$_{0.50}$-REP/TiO$_2$ in the as-sprayed and cured states. (b, d) Representative cross-sectional images of the corresponding coatings on MDF, showing coating thicknesses of approximately 15 and 14 μm, respectively.

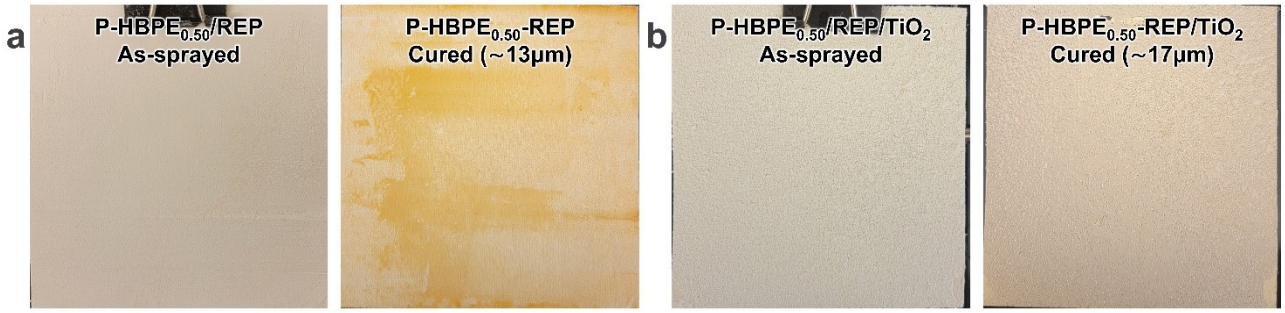

Figure S19. Photographs of basswood sheets spray-coated with (a) P-HBPE$_{0.50}$-REP and (b) P-HBPE$_{0.50}$-REP/TiO$_2$ in the as-sprayed and cured states, with coating thicknesses of approximately 13 and 17 μm after curing, respectively.

18. Cone calorimetric data

Table S5. Cone calorimetric data for $HBPE_{0.50}$-REP, P-$HBPE_{0.50}$-REP, and P-$HBPE_{0.50}$-REP/TiO_2.

Sample	TTI [s][a]	pHRR [kW m^{-2}][b]	THR [MJ m^{-2}] [c]	MARHE [kW m^{-2}][d]	FIGRA [kW·m^{-2}·s^{-1}][e]	TSP [m^2] [f]	CR [%][g]
$HBPE_{0.50}$-REP	13	375.8	64.9	254.8	5.1	6.2	12.1
P-$HBPE_{0.50}$-REP	15	262.1	47.4	180.1	2.6	22.3	19.0
P-$HBPE_{0.50}$-REP/TiO_2	15	209.9	45.6	150.2	3.9	17.7	37.4

[a]TTI: time to ignition; [b]pHRR: peak heat release rate; [c]THR: total heat release; [d]MARHE: maximum average rate of heat emission; [e]FIGRA: fire growth rate index = maximum quotient of HRR(t)/t; [f]TSP: total smoke production; [g]CR: char residue.

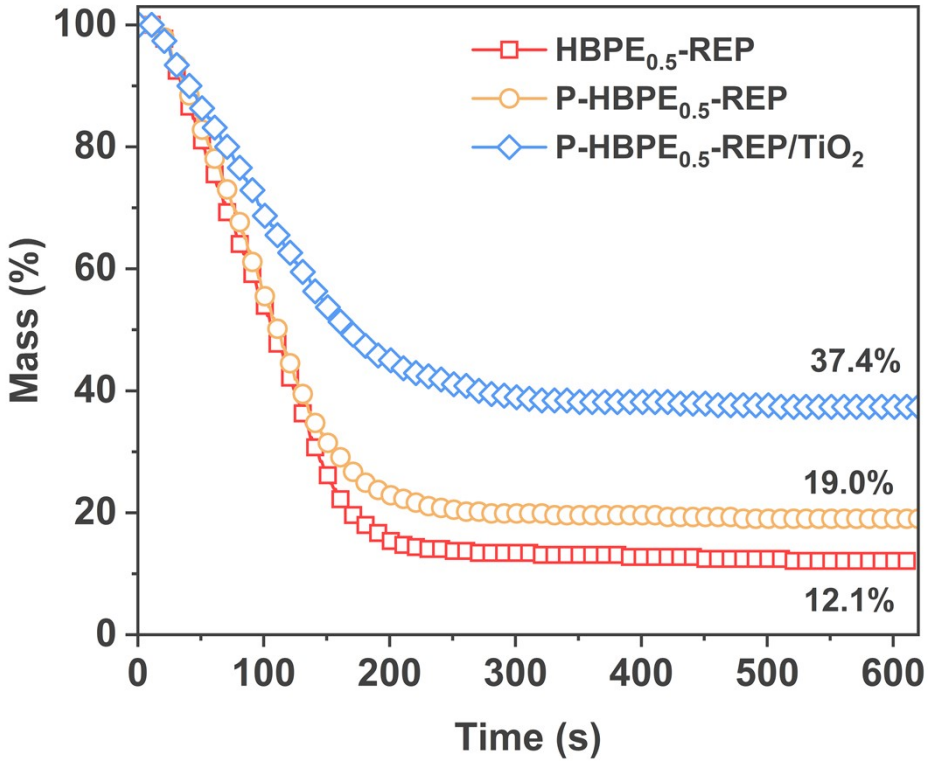

Figure S20. Real-time mass loss curves during cone calorimetry test.

19. Analysis of char residues after cone calorimetry

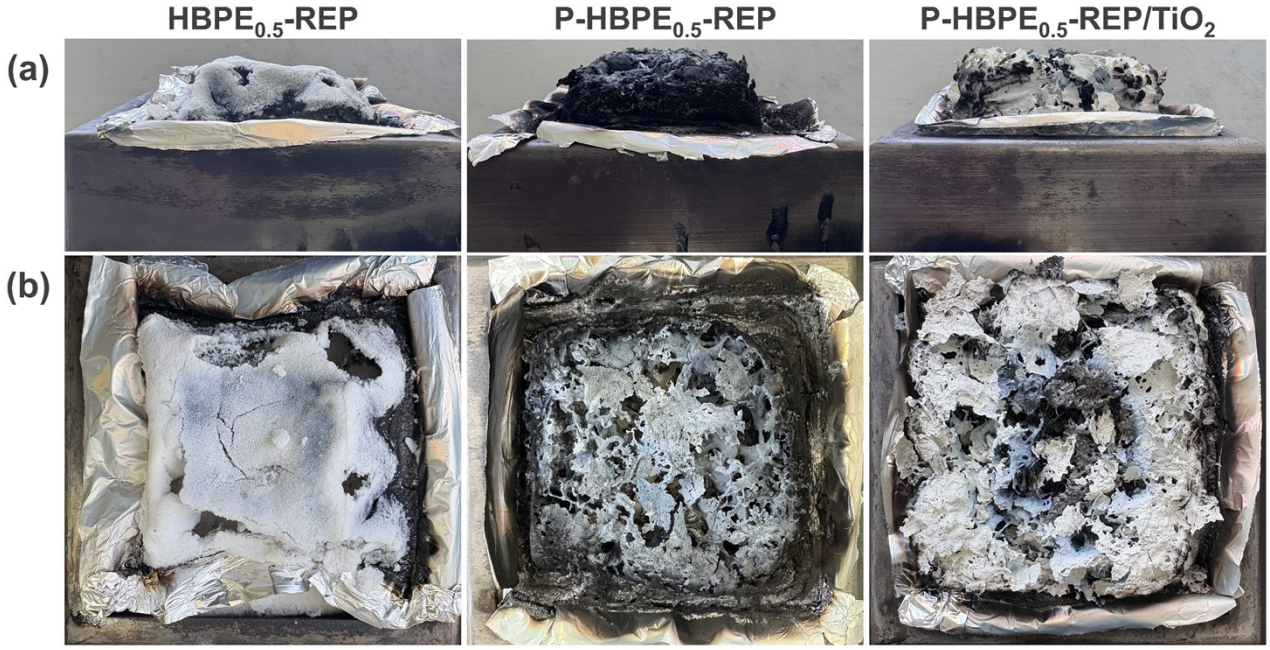

Figure S21. (a, b) Digital photographs for the burning residues of the bulk resins after cone calorimetry.

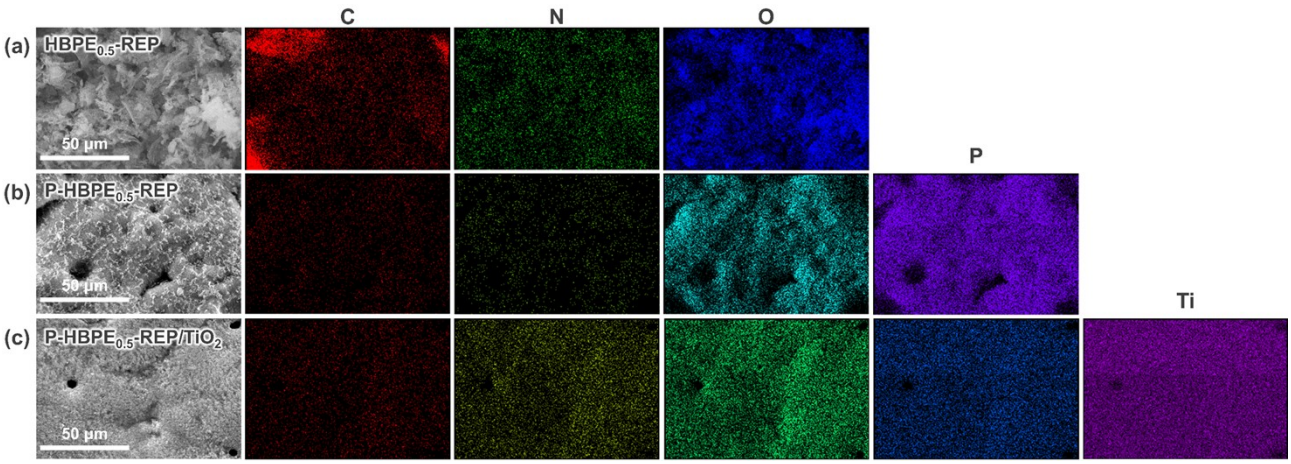

Figure S22. EDS elements mapping images for the burning residues of the bulk resins after cone calorimetry: (a) $HBPE_{0.5}$-REP, (b) P-$HBPE_{0.5}$-REP, and (c) P-$HBPE_{0.5}$-REP/TiO_2.

Table S6. Surface elemental composition of residual chars determined by XPS.

Sample	Element	Start BE	Peak BE	End BE	Height CPS	FWHM eV	Atomic %
$HBPE_{0.5}$-REP	C1s	298.11	284.8	279.31	138577.01	1.53	85.1
	N1s	410.11	399.15	392.31	3980.48	2.38	3.54
	O1s	545.11	532.68	525.31	27493.04	3.11	11.35
P-$HBPE_{0.5}$-REP	C1s	298.19	284.8	279.39	148118.94	1.52	87.81
	N1s	410.19	400.17	392.39	2606.83	3.04	2.2
	O1s	545.19	532.5	525.39	21276.3	2.99	9.05
	P2p	144.19	133.22	124.39	1456.19	2.22	0.94
P-$HBPE_{0.5}$-REP/TiO_2	C1s	298.49	284.8	279.69	99641.41	1.65	73.41
	N1s	410.49	400.33	392.69	4780.66	2.92	3.83
	O1s	545.49	532.27	525.69	33990.28	3.92	18.29
	P2p	144.49	134.04	124.69	2972.26	2.45	2
	Ti2p	475.49	459.38	448.69	15943.99	1.22	2.47

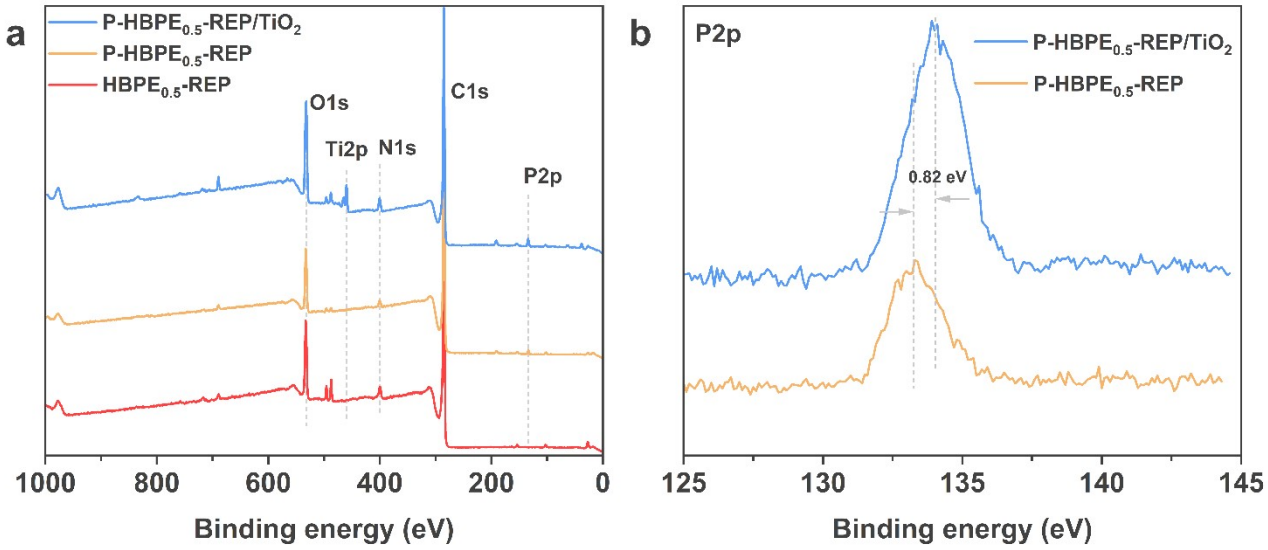

Figure S23. (a) XPS survey spectra of the residual chars from $HBPE_{0.5}$-REP, P-$HBPE_{0.5}$-REP, and P-$HBPE_{0.5}$-REP/TiO_2. (b) High-resolution P2p spectra of the residual chars from P-$HBPE_{0.5}$-REP and P-$HBPE_{0.5}$-REP/TiO_2.

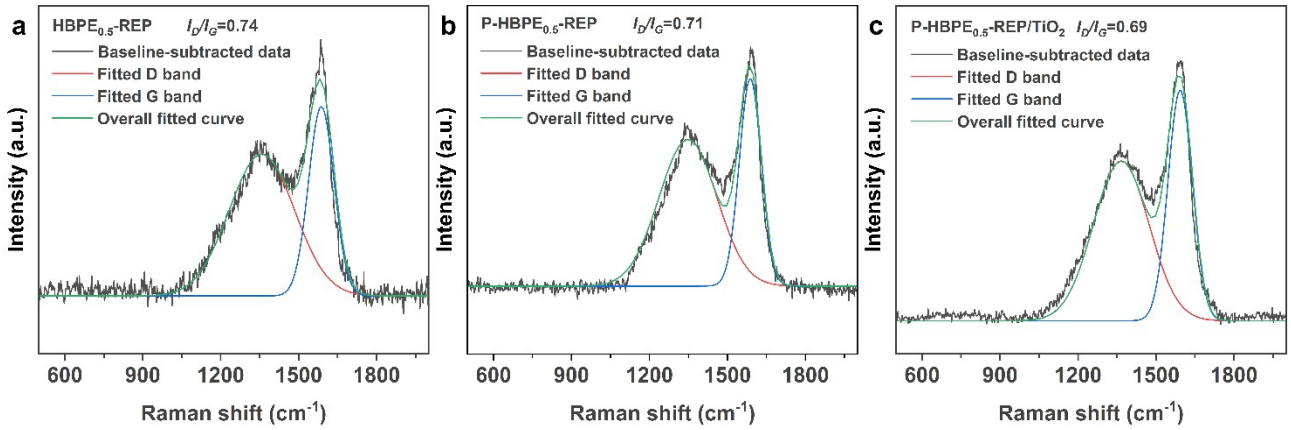

Figure S24. Baseline-subtracted Raman spectra of the residual chars and Gaussian deconvolution of the D and G bands for (a) $HBPE_{0.5}$-REP, P-$HBPE_{0.5}$-REP, and P-$HBPE_{0.5}$-REP/TiO_2, together with the overall fitted curves.

20. Fire protection performance of wood coated with P-HBPE$_{0.50}$-REP-based systems

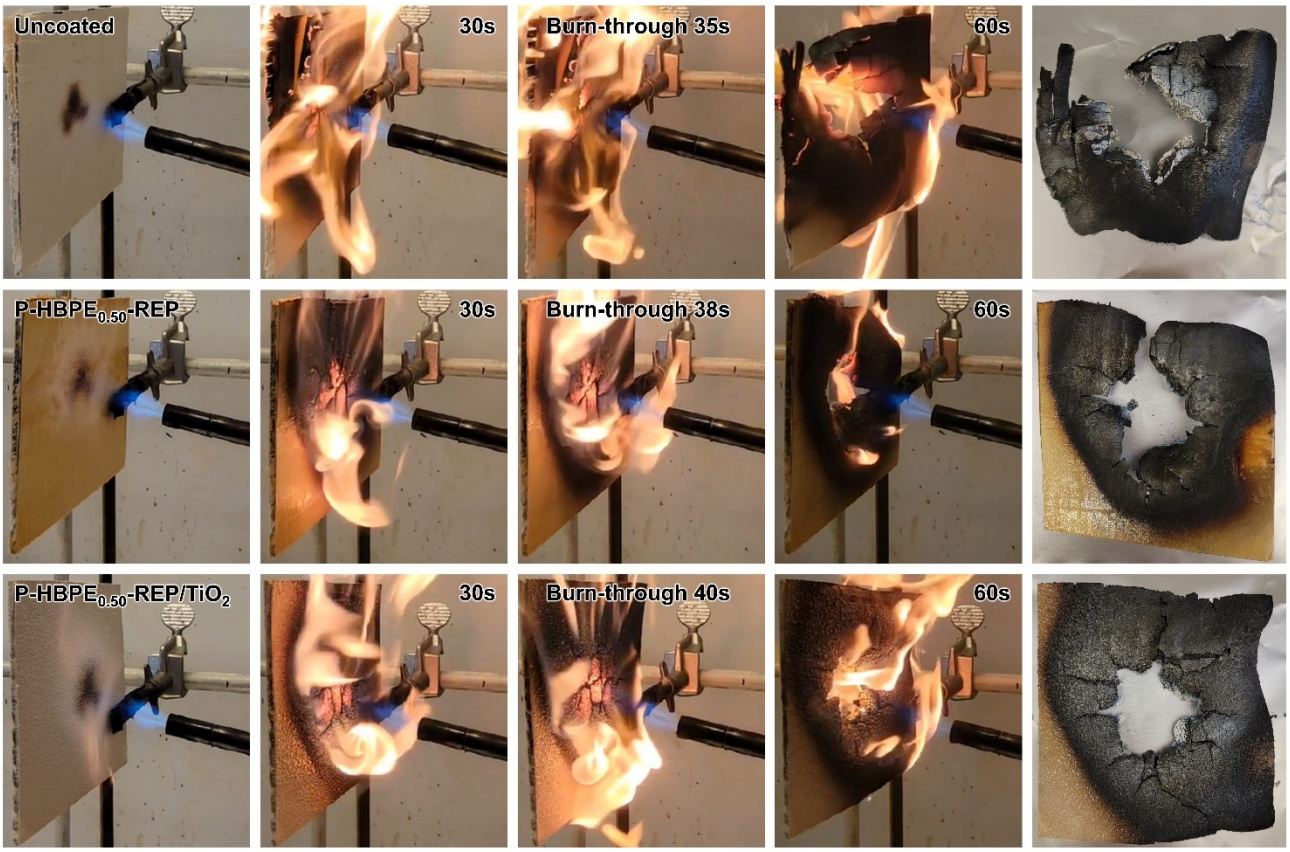

Figure S25. Digital photographs of uncoated wood, P-HBPE$_{0.50}$-REP-coated wood, and P-HBPE$_{0.50}$-REP/TiO_2-coated wood during propane-torch combustion at different exposure times and after burning.

21. Proposed flame-retardant mechanism

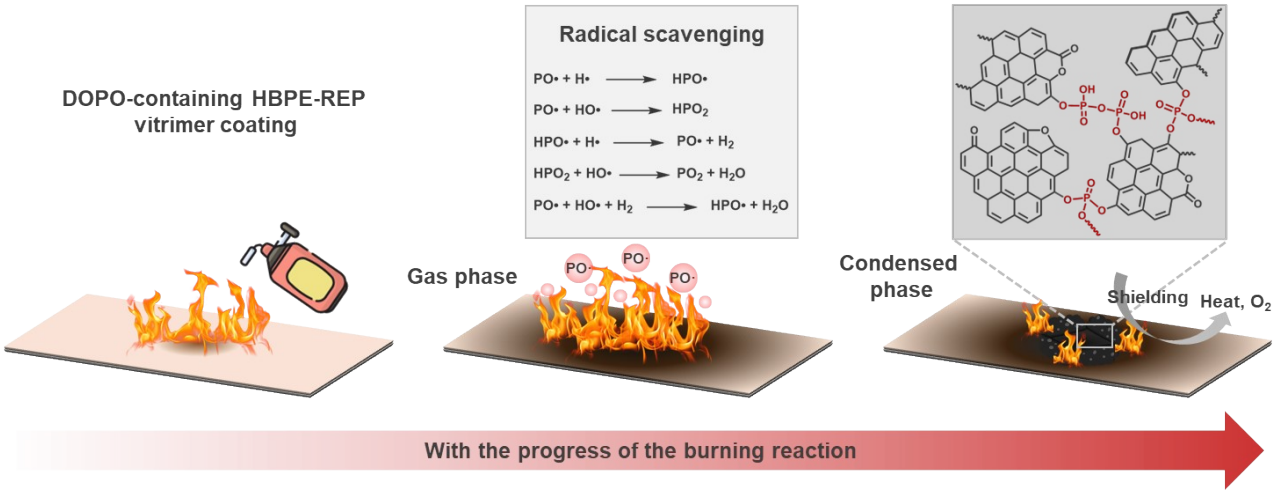

Figure S26. Proposed flame-retardant mechanism of P-HBPE-REP coating.

Table S7. Literature benchmarking of representative polymer-coating systems relevant to the present work, including powder and liquid coatings.

Coating type/Matrix	Sustainability feature	Processing condition	Substrate/Film thickness	Key performance	Ref.
Powder coating/UV-curable cycloaliphatic polyester	VOC-free powder coating; aromatic-reduced/cycloaliphatic design for improved weatherability	Polyester formulation extruded at 100-110 °C; electrostatic spray on steel panels; powder melted at 120 °C for 3 min and then UV-cured	Steel Q-panels / NR	**Service:** adhesion 4B-5B, pencil hardness H-3H, direct impact resistance up to 90 kg·cm, acetone double rubs >50; **Durability:** salt spray rating 9, good gloss retention/weatherability, reduced yellowing vs aromatic controls	1
Powder coating/biobased polyester-REP epoxy	VOC-free; catalyst-free; high biobased content (86.7-90.4 wt%)	Melt-compounded at 100 °C, 5 min; electrostatic spraying; cured at 180 °C, 20 min	Steel/ ~80 μm	**Service:** adhesion 5B, hardness H, MEK >250, impact 15.7-101.9 lb·in; **Healing:** up to 85.7% at 200 °C, 10 min without pressure (100% under 0.37 MPa)	2
Powder coating/MWCNTs-PTFE-PEEK superhydrophobic thermoplastic coating	VOC-free; eco-friendly powder coating; solvent-free fabrication	Dry mixing + solid pressure-bonding; electrostatic spraying; cured at 380 °C for 10 min	Al/steel / ~107.6 μm	**Service:** adhesion 5B, strong abrasion durability; **Functional:** superhydrophobicity, stable after 400 °C/12 h and boiling water (100 °C, 180 min)	3
Liquid-coating/epoxy vitrimer	Solvent-free; RT-curable; phosphorus-free; self-healable; recyclable; biodegradable	RT mixing; blade coating; cured at 25 °C for 12 h	Wood / ~100 μm; foams, steel / up to 300 μm	**Service:** strong/durable adhesion. **Healing:** RT self-healing. **Fire safety:** LOI 37.0%, UL-94 V-0; wood reached LOI 35.0%, V-0 at 100 μm. **Sustainability:** degradable and recyclable with retained performance	4
Liquid-coating/UV-curable eugenol-derived thiol–ene network	Biobased; solvent-free; UV-curable; chemically degradable in aqueous alkali	Mixed at 100 °C for 5 min; UV-cured under 500 W Hg lamp for 10 min	Tinplate/150 μm; free film/300 μm	**Service:** tensile strength 10.8 MPa; transmittance >95% at 600 nm. **Fire safety:** UL-94 V-0; PHRR 425 kW/m²; TSP 6.9 m²; coated tinplate backside temperature only 265.5 °C at 5 min. **Sustainability:** fully degraded in 6 M NaOH at 90 °C within 9 h	5
Liquid-coating/epoxy coating cured by biobased HCPVC	Biobased vanillin-derived curing agent	HCPVC dissolved in trace DMF, mixed with DY-E44 (epoxy/carboxyl = 1/0.75), coated on wood; stepwise cured at 80 °C/1 h, 100 °C/1 h, and 120 °C/1 h	Eucalyptus wood/0.50 ± 0.02 mm	**Service:** hardness 4H, adhesion 5B, 40 in.-lb impact, good water resistance, solvent resistance >200 rubs. **Fire safety:** UL-94 V-0, LOI 30.7, char yield 37.1% at 700 °C	6
Powder coating / PET-upcycled P-HBPE/REP	VOC-free; recycled + biobased feedstocks;	Melt-mixed at 80 °C for 2 min; ball-milled and sieved; electrostatic spray-	Steel, Al, MDF,	**Service:** smooth transparent coating, 2H hardness, 5B adhesion, scratch self-healing	This work

vitrimer	phosphorus-containing self-healable coating	coated; cured at 150 °C for 20 min	basswood plywood / ca. 20 μm	efficiency of 100% after 180 °C/30 min. **Fire safety:** LOI 34.5%, UL-94 V-0, pHRR and THR reduced by 30.3% and 27.0%, respectively; effective fire protection was also demonstrated on steel, MDF, and basswood plywood.

Note: Owing to differences in coating chemistry, substrate, film thickness, and testing protocols, the comparison is intended to provide a qualitative-to-semiquantitative positioning rather than a strict one-to-one ranking.

Table S8. Qualitative sustainability positioning of the present PET-upcycled powder-coating system relative to conventional fossil-based powder coatings.

Aspect	Present coating system	Conventional fossil-based powder coatings	Implication/comment
Feedstock origin	Incorporates recycled PET-derived THETA and a biobased resveratrol-derived epoxy, resulting in >55% sustainable carbon content	Typically derived predominantly from virgin petrochemical feedstocks	Indicates reduced reliance on virgin fossil carbon in the present system.
Application-stage emissions	Applied as a solvent-free powder coating, with no solvent emission during coating application	Powder coatings are likewise applied in a solvent-free manner during coating deposition.	The present system retains the inherent low-emission application advantage of powder coatings rather than introducing a unique benefit at this stage.
Curing and processing demand	Cured at 150 °C for 20 min under a practically relevant powder-coating schedule	Commercial powder coatings are also generally designed for practical thermal curing	No quantitative basis is currently available to claim reduced processing-energy demand; however, the present system is cured under practically relevant conditions without an unusually demanding thermal schedule.
Potential use-phase sustainability benefit	Self-healing capability and enhanced fire protection may help extend coating service life and reduce recoating frequency	Self-healing is generally absent, and intrinsic flame retardancy depends on formulation design	Suggests potential use-phase material-efficiency benefits, although these effects have not yet been quantified.
Formulation safety and toxicity considerations	Intrinsic flame retardancy is achieved without externally added halogenated flame retardants; however, the current laboratory synthesis still involves DMF, xylene/toluene, and an organotin catalyst	Formulations are highly variable and often proprietary, and may differ substantially in resin chemistry, curing agents, and additive package	A straightforward toxicity comparison cannot be made; the present system presents both formulation-level advantages and synthesis-related limitations.
Assessment boundary and current uncertainty	The present route has only been demonstrated at laboratory scale, and no foreground inventory is yet available for solvent recovery, catalyst substitution, or scale-up	Commercial benchmark systems are often proprietary, and publicly available life-cycle inventory data are usually insufficiently complete for rigorous direct comparison	The environmental implications should therefore be interpreted as qualitative and directional rather than as quantitatively established by formal LCA.

Note: This table is intended to provide a qualitative sustainability positioning of the present coating system rather than a formal life-cycle assessment. A rigorous cradle-to-gate LCA was considered beyond the scope of the present work because reliable foreground inventory data are not yet available for the current laboratory-scale synthesis, while comparable public inventory data for commercial fossil-based powder coatings are generally limited.

1. Hammer, T. J.; Pugh, C.; Soucek, M. D., Ultraviolet-Curable Cycloaliphatic Polyesters Containing Spiroacetal Moieties for Application as Powder Coatings. ACS Applied Polymer Materials 2022, 4 (4), 2294-2305.
2. Zhao, B.; Zhang, Y.; Liu, W.; Gu, S.; Fei, M.; Cao, Y.; Bliss, B. J.; Canterbury, T.; Zhang, J., Biobased Catalyst-Free Polyester–Epoxy Powder Coatings with Self-Healing Functionality. ACS Applied Polymer Materials 2026.
3. Bai, Y.; Zhang, H.; Zhang, H.; Zhu, J.; Shao, Y.; Huang, J., Eco-friendly Superhydrophobic MWCNTs/PTFE/PEEK Powder Coating for Stable Superhydrophobicity in Extreme Environments. ACS Applied Polymer Materials 2025, 7 (19), 13011-13023.
4. Wang, C.; Huo, S.; Ye, G.; Cao, C.-F.; Hong, M.; Pan, Y.-T.; Song, P.; Wang, H.; Wang, T.; Liu, Z., Tick-inspired, self-healing, and strongly-adhesive coatings with biodegradability and phosphorus-free fire retardancy. Journal of Materials Science & Technology 2026, 260, 229-240.
5. Jiang, B.; Ying, J.; Chen, G.; Han, J.; Wang, S.; Wu, S.; Li, S.-N.; Peng, L.; Wu, S.; Guo, Y.; Dai, J., Eugenol-Derived Thiol–Ene Photopolymerization Networks with Exceptional Flame Retardancy, Mechanical Robustness, and Chemical Degradability. ACS Sustainable Chemistry & Engineering 2025, 13 (26), 10019-10028.
6. Huang, Y.; Ma, T.; Wang, Q.; Guo, C., Synthesis of biobased flame-retardant carboxylic acid curing agent and application in wood surface coating. ACS Sustainable Chemistry & Engineering 2019, 7 (17), 14727-14738.